Mon. Not. R. Astron. Soc. **357,** 82–96 (2005) doi:10.1111/j.1365-2966.2005.08612.x

Evolution of the density profiles of dark matter haloes

Darren Reed,[1,2]★ Fabio Governato,[1,3] Licia Verde,[4,5] Jeffrey Gardner,[6] Thomas Quinn,[1] Joachim Stadel,[7] David Merritt[8] and George Lake[9]

[1]*Astronomy Department, University of Washington, Box 351580, Seattle, WA 98195 USA*
[2]*ICC, Department of Physics, University of Durham, Rochester Building, Science Laboratories, South Road, Durham DH1 3LE*
[3]*INAF, Osservatorio Astronomico di Brera, via Brera 28, I-20131 Milano, Italy*
[4]*Department of Physics & Astronomy, University of Pennsylvania, 209 South 33rd Street, Philadelphia, PA 19104-6396, USA*
[5]*Department of Astrophysical Sciences, Princeton University, Peyton Hall, Ivy Lane, Princeton, NJ 08544 USA*
[6]*Pittsburgh Supercomputing Centre, 4400 Fifth Avenue, Pittsburgh, PA 15213, USA*
[7]*Institute for Theoretical Physics, University of Zurich, Winterthurerstrasse 190, 8057, Switzerland*
[8]*Department of Physics, Rochester Institute of Technology, 84 Lomb Memorial Dr., Rochester, NY 14623-5603, USA*
[9]*Department of Physics, PO Box 642814, Washington State University, Pullman, WA 99164-2814, USA*

Accepted 2004 November 5. Received 2004 September 1; in original form 2003 December 21

ABSTRACT

We use numerical simulations in a ΛCDM cosmology to model density profiles in a set of 16 dark matter haloes with resolutions of up to seven million particles within the virial radius. These simulations allow us to follow robustly the formation and evolution of the central cusp over a large mass range of 10^{11}–10^{14} $M_{\odot}$, down to approximately 0.5 per cent of the virial radius, and from redshift of 5 to the present, covering a larger range in parameter space than previous works. We confirm that the cusp of the density profile is set at redshifts of 2 or greater and remains remarkably stable to the present time, when considered in non-comoving coordinates.

Motivated by the diversity and evolution of halo profile shapes, we fit our haloes to the two-parameter profile, $\rho \propto 1/\{(c_\gamma r/r_{\rm vir})^\gamma [1 + (c_\gamma r/r_{\rm vir})]^{3-\gamma}\}$, where the steepness of the cusp is given by the asymptotic inner slope parameter, γ, and its radial extent is described by the concentration parameter, c_γ (with c_γ defined as the virial radius divided by the concentration radius). In our simulations, we find $\gamma \simeq 1.4 - 0.08 \log_{10}(M/M_*)$ for haloes of $0.01\,M_*$–$1000\,M_*$, with a large scatter of $\Delta\gamma \sim \pm 0.3$, where M_* is the redshift dependent characteristic mass of collapsing haloes; and $c_\gamma \simeq 8.(M/M_*)^{-0.15}$, with a large M/M_* dependent scatter roughly equal to $\pm\, c_\gamma$. Our redshift zero haloes have inner slope parameters ranging approximately from r^{-1} (Navarro, Frank and White) to $r^{-1.5}$ (Moore et al.), with a median of roughly $r^{-1.3}$. This two-parameter profile fit works well for all types of haloes in our simulations, whether or not they show evidence of a steep asymptotic cusp. We also model a cluster in power-law cosmologies of $P \propto k^n$, with $n = (0, -1, -2, -2.7)$. Here we find that the concentration radius and the inner cusp slope are both a function of n, with larger concentration radii and shallower cusps for steeper power spectra.

We have completed a thorough resolution study and find that the minimum resolved radius is well described by the mean interparticle separation over a range of masses and redshifts. The trend of steeper and more concentrated cusps for smaller M/M_* haloes clearly shows that dwarf-sized ΛCDM haloes have, on average, significantly steeper density profiles within the inner few per cent of the virial radius than inferred from recent observations.

Code to reproduce this profile can be downloaded from http://www.icc.dur.ac.uk/~reed/profile.html.

Key words: methods: *N*-body simulations – galaxies: formation – galaxies: haloes – cosmology: theory – dark matter.

★E-mail: d.s.reed@durham.ac.uk

1 INTRODUCTION

The mass distribution of dark matter haloes provides a direct probe of the nature of the dark matter particle, as the inner structure of dark matter haloes is particularly sensitive to the dark matter properties. For example, warm dark matter should produce lower density halo cores than cold dark matter (CDM) because of the phase density ceiling introduced by the non-zero thermal velocity of warm particles (e.g. Tremaine & Gunn 1979). The variation of peak halo phase density with halo mass is also dependent on the 'coldness' of the dark matter particle (e.g. Lake 1989, and references therein). Spectroscopic observations of stellar motions in galaxies, lensing properties and X-ray temperature maps of cluster cores each can provide a measurement of the central dark matter distribution in haloes, albeit with some uncertainty inherent in inferring the dark matter distribution from properties of baryons or baryon dominated regions. CDM haloes in *N*-body simulations consistently have a steep central cusp where the density rises as r^{-1} [(Navarro, Frenk & White 1996, 1997, collectively hereafter NFW); Huss, Jain & Steinmetz 1999; Power et al. 2003], $r^{-1.5}$ (Moore et al. 1998, 1999, M99 hereafter; Taylor & Navarro 2001; Governato, Ghigna & Moore 2001; Fukushige & Makino 2001, 2003), or somewhere in between (e.g. Klypin et al. 2001; Hayashi et al. 2003; Navarro et al. 2004; Fukushige, Kawai & Makino 2004). These numerical findings appear in conflict with the most direct observational results. Rotation curves of low surface brightness (LSB) dwarfs consistently yield density profiles with nearly constant density cores (e.g. Flores & Primack 1994; Moore 1994; Salucci & Burkert 2000; de Blok et al. 2001). Studies of more luminous galaxies imply similar problems (e.g. Salucci & Burkert 2000; Salucci 2003; Gentile et al. 2004). The disagreement with rotation curves may indicate an insurmountable problem with CDM models, may be owing to uncertainties in measuring accurate stellar curves at just $\sim$1 per cent of the virial radii (van den Bosch, Robertson & Dalcanton 2000; van den Bosch & Swaters 2001; see, however, e.g. Simon et al. 2003), or may perhaps reflect some systematic bias common to all high-resolution *N*-body simulations. Alternatively, the disagreement may be owing to a problem with common assumptions made when reconstructing mass profiles from circular velocity data (Hayashi et al. 2003). Strong gravitational lensing in clusters can potentially provide a direct measurement of the halo mass profile, and indeed central mass profiles for several lensing clusters have been calculated (Tyson, Kochanski & Dell'Antontio 1998; Shapiro & Iliev 2000; Sand, Treu & Ellis 2002; Gavazzi et al. 2003; Sand et al. 2004), but have yielded conflicting results. Cluster density profiles inferred from *Chandra* luminosity–temperature mapping have steep cusps that are inconsistent with the flat cores observed from LSB rotation curves (Lewis, Buote & Stock 2003), though this method is sensitive to models of the intracluster gas. In summary, many observational studies suggest a flatter profile than predicted by CDM models, but observations have not yet converged upon a basic shape of the density profile (e.g. Jimenez, Verde & Oh 2003).

NFW found that CDM haloes have a 'universal' density profile that is independent of mass, cosmological parameters and the initial density fluctuation spectrum with significant scatter from halo to halo

$$\rho = \frac{\rho_{\rm s}}{(r/r_{\rm s})(1 + r/r_{\rm s})^2}, \tag{1}$$

where $r_{\rm s}$ and $\rho_{\rm s}$ is a characteristic inner radius (the concentration radius) and inner density, respectively. Fukushige & Makino (1997), based on a single halo with $\sim 10^6$ particles, as opposed to the $\sim 10^4$ particles of the NFW study, found a profile with slope between r^{-1} and r^{-2}. M99, using results from a series of six $\sim 10^6$ particle haloes, also found a profile steeper than r^{-1}, and proposed the following profile:

$$\rho = \frac{\rho_{\rm s}}{(r/r_{\rm s})^{1.5}\left[1 + (r/r_{\rm s})^{1.5}\right]}. \tag{2}$$

The NFW and M99 profiles are both specific cases of a three-parameter profile family proposed by Hernquist (1990), and further developed by Zhao (1996). The highest resolution haloes to date are a series of eight clusters, several with $\sim$20–30 $\times$ 10^6 particles (Fukushige, Kawai & Makino 2004), which have central slopes steeper than NFW and shallower than M99.

The level of 'universality' of the density profile is a matter of debate (e.g. Tasitsiomi et al. 2004). Jing & Suto (2000, 2002), found central density cusps of $r^{-1.1}$, $r^{-1.3}$ and $r^{-1.5}$ for a simulated halo with cluster, group and galaxy mass, respectively. A similar range of inner slope values was found in a recent set of high-resolution haloes (Hayashi et al. 2003; Navarro et al. 2004). The central cusp is especially sensitive to flattening caused by poor resolution or other numerical effects (e.g. Moore et al. 1998), so slightly different numerical techniques might produce significantly different density profiles, making it sometimes difficult to compare results of different authors. The appearance of near universality in many previous studies could be owing to the fact that most simulations have modelled objects in the range of galaxies to clusters; in this mass range the effective slope of the linear power spectrum [n, where $P(k) \propto k^n$] is $n \simeq -2$, implying cusps of roughly NFW slope (Syer & White 1998; Subramanian, Cen & Ostriker 2000). Ricotti (2003), using a large set of haloes with 10^4 to 10^5 particles, found considerably flatter cusps for high-redshift low-mass haloes, with $r^{-0.5}$ at $z \gtrsim 10$ for $10^8\ h^{-1}\ {\rm M}_\odot$. Flat, low-mass haloes match model predictions (Syer & White 1998; Subramanian et al. 2000), wherein the central slope varies as $r^{(9+3n)/(5+n)}$. See, however, Moore et al. (2001), who find a $r^{-1.3}$ cusp in a $10^8\ h^{-1}\ {\rm M}_\odot$ halo at a redshift of 4. In CDM models, any dependence on n would be manifested as a dependence on halo mass. In the ΛCDM model, n asymptotically approaches -3 for low-mass haloes. As n nears -3, M_*, the characteristic mass of collapsing haloes as a function of scale factor (see Section 4.3) diverges, so haloes of all masses collapse nearly simultaneously. If one models halo formation as the assembly of spherically symmetric shells of material whose density is largely determined by the scale factor of the universe, then the density profile should be shallower when n nears -3.

The characteristic radius, $r_{\rm s}$, indicates the size of the central density region and is usually defined in terms of the concentration parameter, $c = r_{\rm vir}/r_{\rm s}$. NFW, as well as a number of other authors found that the concentration radius decreases with halo mass, even for power-law cosmologies where n is constant. This agrees with other simulations (e.g. Bullock et al. 2001a; Eke, Navarro & Steinmetz 2001), and also with predictions based on the halo model wherein non-linear properties are predicted starting from Press & Schechter (1974) theory (e.g. Huffenberger & Seljak 2003). The concentration dependence on mass becomes weaker when n is closer to -3 (Eke et al. 2001).

In spherically symmetric infall models, concentration should increase with lower mass because lower mass haloes form early, when the universe is more dense, so their central regions are assembled with comparatively higher densities than their outer regions. This should give them higher characteristic central densities, or equivalently, higher concentration parameters (e.g. Eke et al. 2001, and references therein). Eke et al. (2001) and Bullock et al. (2001a)

utilize spherical infall models to predict that halo concentration should decrease with redshift for a given mass for similar reasons. The spherical infall model also gives an intuitive prediction for trends in central slope at a given radius. If halo mass is increasing rapidly with scale factor, then a shallow central slope would be expected because accreting matter will all have a relativity similar physical density. Similar, but perhaps more physically motivated, are merger models (Syer & White 1998; Subramanian et al. 2000), which describe the evolution of the halo density profile as a result of hierarchical halo formation. In the merger models, when smaller satellites merge with the main halo, their orbits will decay via dynamical friction, and tidal stripping will add their mass to the parent halo. The inner slope is then set by the dependence of the concentration (or equivalently, the characteristic density) on satellite mass, and so can be predicted from n. In general, if small haloes formed early, as is the case if $n \sim 0$, they should be dense, which should yield steeper central slopes because their orbits can decay to smaller radii before being tidally disrupted (Syer & White 1998).

Initial works on halo mass profiles suffered from poor resolution that made it difficult to evaluate the central slopes in haloes with high concentrations (i.e. at galaxy scales). In addition, samples with higher resolution but with limited statistics could not study trends over a large mass range, different cosmologies, and were unable to evaluate the intrinsic amount of cosmic scatter. Finally, a large dynamical range and high-mass resolution at high redshift are necessary to follow the early assembly of the central part of dark matter haloes. This is particularly difficult for small-mass haloes that have higher concentrations, form earlier, and then need to be evolved by several internal dynamical times. A careful choice of the softening, force errors and number of time-steps is then necessary to avoid introducing spurious numerical trends.

In this work, we improve upon previous studies by modelling a large set of high-resolution haloes and following their evolution over a wide range in mass and redshift parameter space. We present a set of high-resolution simulations covering three orders of magnitude in mass, from $2 \times 10^{11}\ h^{-1}\ \mathrm{M}_{\odot}$ to $2 \times 10^{14}\ h^{-1}\ \mathrm{M}_{\odot}$. This allows us to search for potential mass dependent trends in halo profiles. Our highest resolution haloes have 4 million and 7 million particles within the virial radius, respectively. Ten of our haloes are from CUBEHI, a single simulation of a cosmological volume at uniform resolution. This allows us to analyse cosmological scatter in profile shapes with a uniform method not subject to systematic uncertainties associated with differing numerical parameters. Furthermore our haloes are resolved with several hundreds of thousands of particles to redshift of 2 and, in a few cases, to redshift of 4 or higher.

2 NUMERICAL TECHNIQUES

2.1 The simulations

We use the parallel KD (balanced binary) Tree (Bentley 1975) gravity solver PKDGRAV (Stadel 2001; see also Wadsley, Stadel & Quinn 2004) for all of our numerical simulations. Initial conditions for the simulations are set by mapping particles on to a random realization of the mass power spectrum, which is extrapolated to a sufficiently high redshift, z_{start}, that particle overdensities are safely in the linear regime. For higher resolution within a single halo, we use a 'renormalized volume' technique of nested resolution regions, which has been successful in a number of cosmological simulations (e.g. Katz & White 1993; Ghigna et al. 1998). First, a low-resolution cosmological simulation is completed. Next, a halo of interest is identified. To minimize sampling bias, volume-renormalized haloes are selected by mass with the only additional constraint that they not lie within close proximity (2–$3r_{\mathrm{vir}}$) to a halo of similar or larger mass. Then, the initial conditions routine is run again to add small-scale power to a region made up of high-resolution particles that end up within approximately two virial radii of the halo centre, while preserving the original large-scale random waves. This process is iterated in mass resolution increments of a factor of 8 until the desired resolution is achieved. We have verified that the high-resolution haloes are free from significant contamination by massive particles.

All of the simulations model a ΛCDM cosmology with $\Omega_{\mathrm{m}} = 0.3$ and $\Lambda = 0.7$. We normalize the density power spectrum of our initial conditions such that σ_8 extrapolated to redshift of 0 is 1.0, consistent with both the cluster abundance (see e.g. Eke, Cole & Frenk 1996 and references therein) and the *WMAP* normalization (e.g. Bennett et al. 2003; Spergel et al. 2003). We use a Hubble constant of $h = 0.7$, in units of $100\ \mathrm{km\ s^{-1}\ Mpc^{-1}}$, and assume no tilt (i.e. a primordial spectral index of 1). To set the initial conditions, we use the Bardeen et al. (1986) transfer function with $\Gamma = \Omega_{\mathrm{m}}(z = 0)\, h$. See Reed et al. (2003) for further details on the uniform resolution CUBEHI run.

Our high-resolution simulations are listed in Table 1. For the volume-renormalized runs, we list the effective particle number of the highest resolution region rather than the actual particle number. Softening choices are chosen based on empirical studies (e.g. Moore et al. 1998; Power et al. 2003). Force softenings are $r_{\mathrm{soft}} = 5\ h^{-1}$ kpc for the uniform resolution CUBEHI run, and $r_{\mathrm{soft}} = 1.5$ per cent times the mean inter-particle spacing for the volume-renormalized runs. Long range forces are calculated by hexadecapole expansion of the potentials of distant tree nodes (or 'cells') that subtend an angle

Table 1. Summary of our halo sample at redshift zero. For volume-renormalized runs, the mass and particle number of the central halo is listed. $N_{\mathrm{p,eff}}$ is the effective particle number based on the high-resolution region for renormalized runs.

	M_{Halo}	$N_{\mathrm{p,halo}}$	$N_{\mathrm{p,eff}}$	r_{soft} (h^{-1} kpc)	$\Theta(z > 2)$	$\Theta(z < 2)$	z_{start}	L_{box} (h^{-1} Mpc)	
CUBEHI	0.7–2.1×10^{14}	0.6–1.6×10^{6}	432^3	5	0.7	0.8	69	50	10 clusters
GRP1	4×10^{13}	7.2×10^{6}	1728^3	0.625	0.5	0.7	119	70	Fornax mass
CL1	2.1×10^{14}	4.6×10^{6}	864^3	1.25	0.5	0.7	119	70	Cluster
GAL1	2×10^{12}	0.88×10^{6}	2304^3	0.469	0.5	0.7	119	70	Milky Way
GRP2	1.69×10^{13}	0.38×10^{6}	864^3	1.25	0.5	0.7	119	70	Group
DWF1	1.88×10^{11}	0.64×10^{6}	4608^3	0.234	0.5	0.7	119	70	Two dwarfs
	1.93×10^{11}	0.66×10^{6}							
$n = 0$	1.9×10^{14}	0.54×10^{6}	432^3	2.5	0.5	0.7	799	70	$P \propto k^{0}$
$n = -1$	2×10^{14}	0.55×10^{6}	432^3	2.5	0.5	0.7	269	70	$P \propto k^{-1}$
$n = -2$	1.6×10^{14}	0.45×10^{6}	432^3	2.5	0.5	0.7	99	70	$P \propto k^{-2}$
$n = -2.7$	2.9×10^{13}	0.82×10^{5}	432^3	2.5	0.5	0.7	79	70	$P \propto k^{-2.7}$

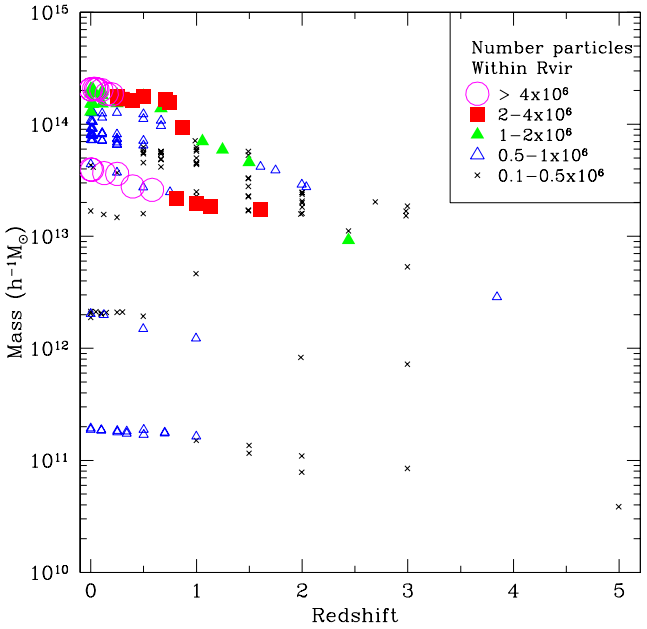

Figure 1. Our set of haloes for density profile analyses, including lower resolution tests.

less than the cell opening angle, Θ, chosen to be consistent with tests by Stadel (2001). Θ is set to be smaller at high redshift, when force errors owing to long-range gravitational forces can have a larger contribution to total forces as the density field is more uniform. Timesteps for the CUBEHI run are constrained to $\Delta t < 0.2\sqrt{r_{\rm soft}/a}$, where a is the magnitude of the acceleration of a given particle, for the CUBEHI run, and $\Delta t < 0.175\sqrt{r_{\rm soft}/a}$ for all other runs. These time-steps are consistent with convergence tests for variable time-step runs by Power et al. (2003), where $\Delta t \lesssim 0.2\sqrt{r_{\rm soft}/a}$ is found to be sufficient for the central regions of haloes. The number of periodic replicas, $n_{\rm r}$ is 1 for all simulations; $n_{\rm r}$ determines the number of copies of the box for gravity calculations, and hence the accuracy of the periodic force. Starting redshift, $r_{\rm soft}$, Θ and n_r are all tested for the CUBEHI run in Reed et al. (2003).

For our volume-renormalized galaxy, group and cluster runs, we have analysed lower resolution runs which we use for a numerical resolution study. In the interest of limiting our study to only the highest resolution haloes, we only calculate density profiles for the 10 most massive haloes in our CUBEHI run, each of which has $\sim 10^6$ particles. For similar reasons we only follow the evolution of haloes to redshifts where their particle number exceeds 10^5. In Fig. 1, we plot the properties of the full sample of haloes that we analyse, including our low-resolution versions of the renormalized runs GAL1, GRP1 and CL1 when they exceed 10^5 particles. The $n = 0, -1, -2$ and -2.7 runs are used to study the effects of power index spectral slope on halo structure. The initial power spectrum for these runs is given by $P \propto k^n$ normalized to the same σ_8 as all other runs. These power spectra are based on the same random waves as run CL1.

2.2 The analysis

Our virialized haloes are selected with the (SO) algorithm (Lacey & Cole 1994) utilizing the spherical tophat model of Eke et al. (1996) in which the ΛCDM virial overdensity, $\Delta_{\rm vir}$, in units of critical density is approximately 100. To follow the evolution of an individual halo, we 'mark' a few hundred particles at the density peak of the halo at $z = 0$ and trace those particles back to higher redshifts, when they are in the core of the largest progenitor haloes. When there are multiple progenitors, we use the progenitor with the deepest potential.

To calculate density profiles without excessive particle noise, we developed a novel kernel-based algorithm[1] (Merritt & Tremblay 1994); see Appendix for a full description. Both the width and the shape of the kernel are varied with radius; the variation in shape is significant near the origin, where a symmetric kernel would 'overflow' the $r = 0$ boundary. The window width must be carefully chosen to reduce Poisson noise ('variance') without oversmoothing ('biasing') the profile. In general, it may be shown (e.g. Scott 1992, p. 130) that when the window width is chosen to minimize the mean square error of the estimate, most of the error will come from the variance. Window widths large enough to eliminate the 'wiggles' will generally bias the slope. In addition, the window width should vary with local particle density (Abramson 1982), roughly as $\rho^{-1/2}$. We used a kernel window width that varied as $r^{0.5}$ set at $h_{0.1} = 0.005 r_{\rm vir}$ at $0.1 r_{\rm vir}$ as it yields profiles and profile slopes in good agreement with binned profiles created with TIPSY[2]), and it preserves the central cusp and major substructure.

3 RESOLUTION CRITERIA

In this section, we utilize lower resolution versions of our renormalized-volume simulations to examine several resolution criteria. Previous authors have proposed empirical and theoretical criteria to define the minimum radius at which the density profile can be considered to be 'resolved' (see Diemand et al. 2004 and references therein, whose discussion we summarize here). The main numerical issue is the discreteness caused by the fact that N-body particles are extremely massive compared to dark matter candidates in the 'real' universe. This discreteness means that particles will undergo two-body interactions, which change their velocity by a significant amount. Two-body relaxation effects vanish as $N_{\rm p}$ approaches infinity. The two-body relation time, defined as the time it takes for particle energy to change by order unity, is shortest near halo centres where density is high. In CDM haloes, two-body interactions tend to add energy to the low-velocity cusp particles, so two-body relaxation has the effect of flattening the inner cores of simulated haloes. After several Hubble times, haloes become nearly isothermal and the energy transport reverses direction. Power et al. (2003) and Fukushige & Makino (2001) have considered the relaxation rate at $z = 0$ and found that haloes are resolved down to radii where the relaxation time is equal to the Hubble time and three Hubble times, respectively. Moore et al. (1998) and Ghigna et al. (2000) offer an empirical fit finding that the minimum resolved radius is $r_{\rm min} \simeq l_{\rm mean}/2$ where $l_{\rm mean} = (4/3)^{1/3} N_{\rm p}^{-1/3}$, based on simulations of identical haloes at different resolutions; see Splinter et al. (1998) and references therein for discussions relating resolution to mean particle spacing. As most two-body relaxation occurs early, when particles are in small haloes, particles in higher mass haloes can suffer significantly more relaxation (Diemand et al. 2004). This is owing to the later formation time of massive haloes, which means that their particles have spent more time in small $N_{\rm p}$ progenitors where two-body relaxation is larger (Diemand et al. 2004). We therefore test our resolution criteria over a range of masses.

[1] Code available at http://www.rit.edu/~drmsps/inverse.html
[2] TIPSY is available from the University of Washington N-body group: http://hpcc.astro.washington.edu.

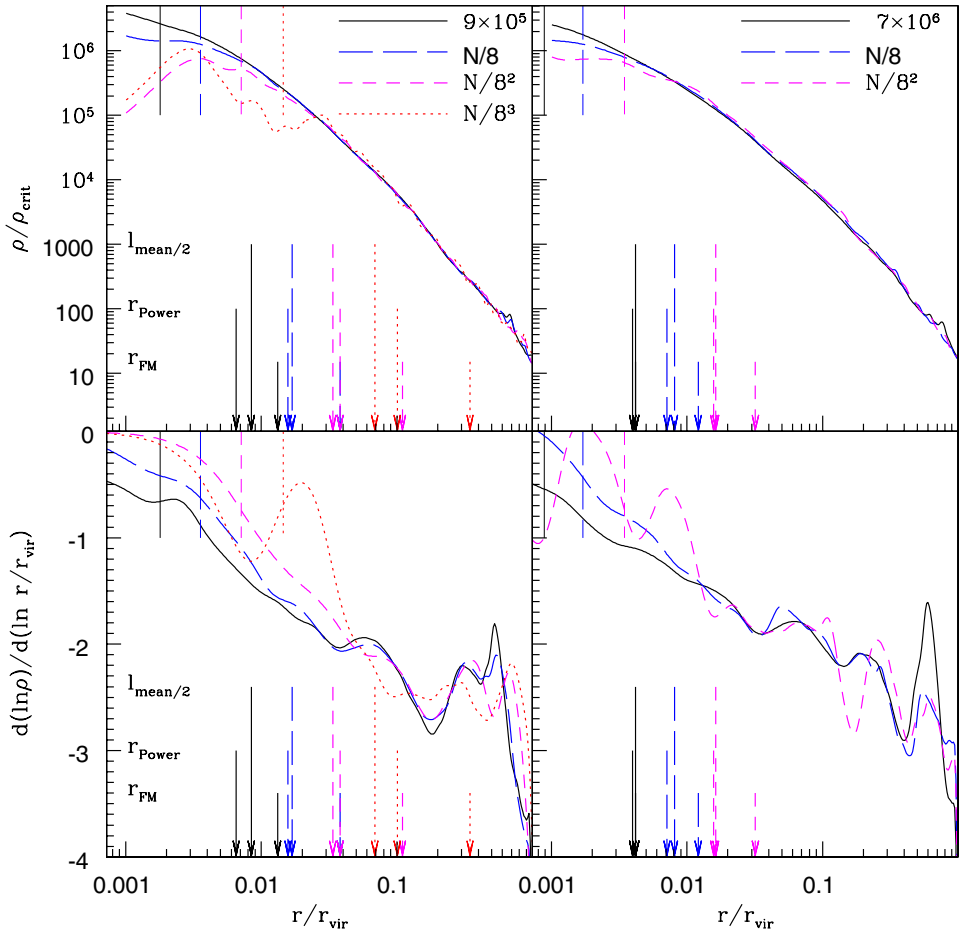

Figure 2. Top panels: density profiles of our galaxy halo (GAL1, left) and our highest resolution halo (GRP1, right) at multiple resolutions. Long arrows show resolution criteria from Moore et al. (1998); medium arrows show Power et al. (2003) criteria; and short arrows show Fukushige & Makino (2001) criteria. Softening is indicated by vertical lines at top of plot windows. Profiles are constructed via a kernel estimator (Appendix). Bottom panels: derivative of the density profile of above haloes at the same resolutions. Density slopes are calculated using a rolling average of $\Delta\, r/r_{vir} \simeq \pm 30$ per cent.

We use identical haloes of varying resolution to empirically identify radii we consider to be well resolved and compare our results with other resolution studies. Fig. 2 shows the density profiles of our galaxy and group for which we have multiple resolutions and indicates the resolution criteria from the above studies. We have made similar resolution studies of cluster CL1. In each case, none of the three resolution underestimates the radii of divergence between the point of divergence between lower and higher resolution haloes over the full mass range. However, the Power et al. and Fukushige & Makino criteria are more conservative for our lower resolution haloes, as they scale more steeply with particle number. Fig. 2 also shows the slopes of the density profiles, $\mathrm{d}\ln\rho/\mathrm{d}\ln(r/r_{vir})$, for the same haloes. To reduce noise, profile slope is calculated based on a rolling average of the kernel-based density profile of roughly $\pm$ 30 per cent in radius.[3] This slope estimation is sufficient for our purposes; however, we note that an optimal method of obtaining low-noise profile slopes is to compute the density derivative directly from a kernel-based density profile that was made using a larger kernel window. The profile slopes seem more sensitive to particle resolution, and thus appear to be accurate down to minimum resolved radii that are ∼50 per cent larger than inferred from the density profiles. At low particle numbers, both Power et al. and sometimes the Fukushige & Makino criteria appear to be over conservative, which suggests that because of their steeper particle number dependence, these criteria may not be conservative enough for haloes with very large N_p values. All of our haloes seem well resolved down to a radius a little larger than $l_{mean/2}$. We thus utilize $r_{min} = N_p^{-1/3}$, which is 25 per cent larger than $l_{mean/2}$. This empirical criterion seems to best match the dependence of r_{min} on particle number in our simulations. We note that one should not expect this criteria to be valid for haloes with vastly different central densities or particle numbers than modelled here, as the relation between resolved radius should depend on the central halo density and other physical properties in addition to particle number. We have performed similar resolution tests of $z = 1$ outputs, where it appears that most haloes are resolved to slightly better than $N_p^{-1/3}$, probably because particles have had less time to undergo two-body interactions. At this high redshift, the Power et al. formula still gives a conservative resolution limit, but the Fukushige & Makino criteria becomes less conservative than $l_{mean/2}$ for our highest particle numbers. In summary, the minimum

[3] As the kernel density estimate is a continuous function of radius, a better way to compute the derivatives would have been via analytical differentiation of $\hat{v}(r)$, using a somewhat larger window width to compensate for the increased variance of the derivative as compared with the function itself (e.g. Scott 1992, p. 131). We recommend that this procedure be followed in the future, though it has no significant effects on our results.

resolved radius of the density profile is well described by $N_p^{-1/3}$ for a wide range of halo masses and redshifts, so we adopt this criteria for the remainder of the paper.

4 RESULTS

4.1 The full halo sample

In Fig. 3, we present a plot of the density profile of all of our haloes at redshifts of 0 and 1. Large substructure is apparent in the profiles which have been constructed with the kernel algorithm described earlier. Each halo has a unique density profile, even in the inner regions where there is little substructure. The cusp size and slope vary from halo to halo. The redshift one profiles are normalized in terms of the redshift zero virial radius and critical density in physical (non-comoving) units, and are plotted out to the $z = 1$ virial radius. There is little evolution of the profile between redshift of 0 and 1. In Fig. 4, we plot the $z = 0$ slopes of the same density profiles, $\mathrm{d}\ \ln\rho/\mathrm{d}\ \ln(r/r_{\rm vir})$, which is calculated based on a rolling fit of approximately $\pm$ 30 per cent in radius. Substructure is prominent in the outer regions of each halo. Only a few of the halo density profiles appear to converge to an asymptotic inner slope; the rest continually flatten all the way down to the innermost resolved radii, though at a rate generally consistent with an asymptotic slope parameter of r^{-1} or steeper. The NFW and M99 curves are plotted for the best-fitting concentration parameters. The innermost slope at the inner resolution limit ranges between $r^{-1.1}$ and $r^{-1.7}$, which implies that the halo to halo cosmic scatter in slope is approximately bounded by the NFW and M99 profiles.

In Fig. 5, the $z = 0$ halo density slopes are plotted versus a two-parameter fit where the inner asymptotic slope parameter is allowed to vary in addition to the concentration parameter. The density is

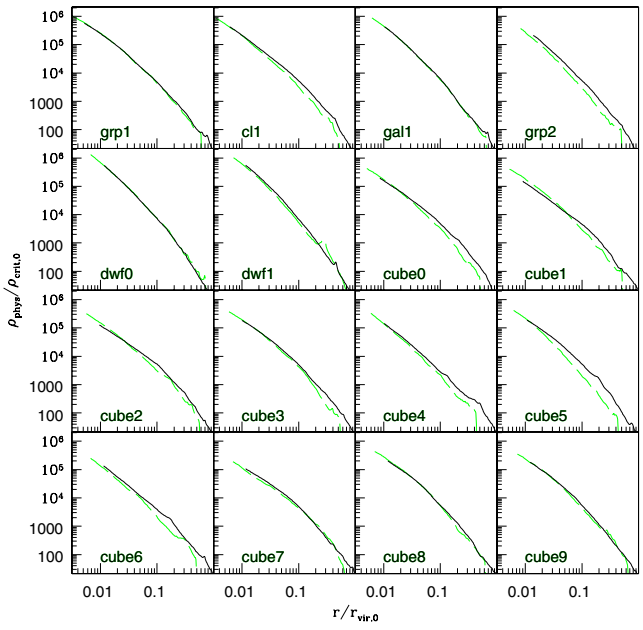

Figure 3. Density profiles of our 16 haloes sample for at $z = 0$ (solid) and $z = 1$ (dashed). Here we rescale the $z = 1$ profiles in physical (non-comoving) coordinates normalized to the critical density and virial radii at $z = 0$ such that a value of $r/r_{\rm vir,0}$ corresponds to the same non-comoving distance from the halo centre at all redshifts. Profiles are plotted to the minimum resolution criteria of $N_p^{-1/3}$.

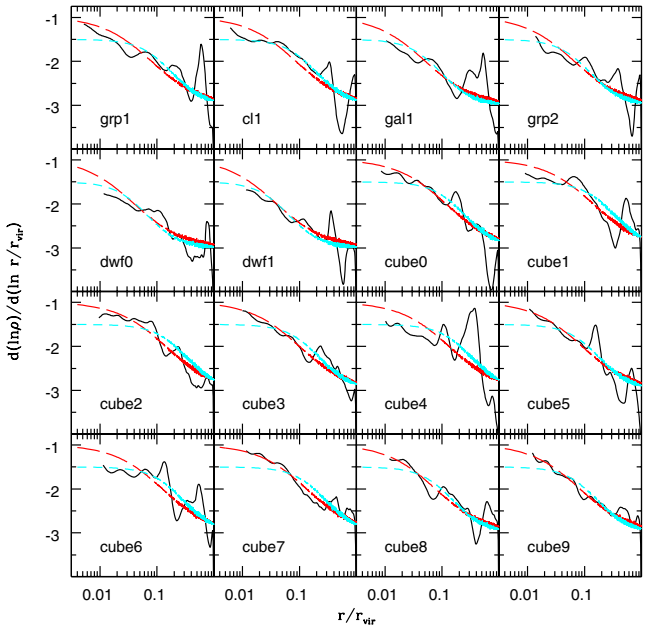

Figure 4. Density profile slopes of our 16 haloes sample for at $z = 0$. The best-fitting concentration NFW (long dashed) and M99 (short dashed) profile slopes are plotted. Profiles are plotted to the minimum resolution criteria of $N_p^{-1/3}$. Slope is calculated based on a rolling fit of $\pm$30 per cent radial width.

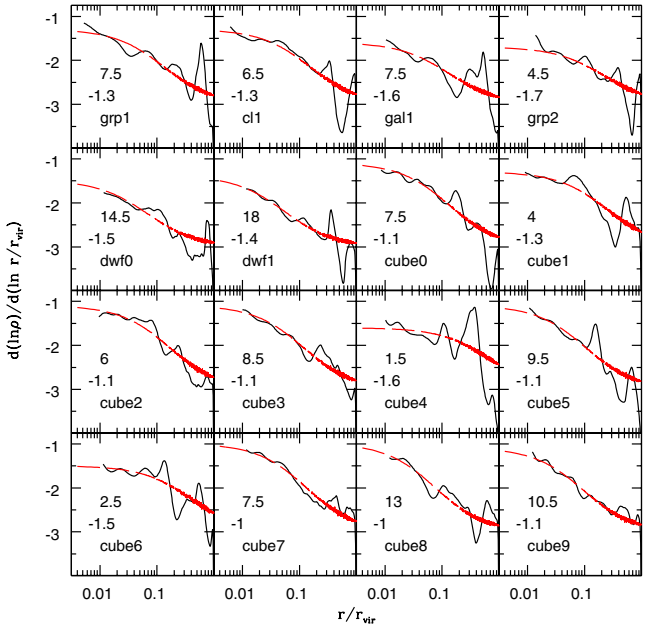

Figure 5. Density profile slopes of our 16 haloes sample at $z = 0$. The long dashed curve shows the results of a two-parameter density profile fit in which both the inner slope parameter, γ, and the concentration parameter, c_γ, are allowed to vary. The top number in each window is the best-fitting c_γ, and the bottom is the value of the best-fitting $(-)\gamma$.

thus given by

$$\rho = \frac{\rho_{\rm s}}{(c_\gamma r/r_{\rm vir})^\gamma [1 + (c_\gamma r/r_{\rm vir})]^{3-\gamma}}, \qquad (3)$$

where γ is the asymptotic inner slope parameter and c_γ is the concentration parameter obtained when γ is a free parameter. This

Table 2. Our best-fitting concentration parameters for the NFW profile (column 3) and the M99 profile (column 5) followed by their respective pseudo-χ^2 per degree of freedom goodness of fits at redshift 0. Columns 7 and 8 are for a two-parameter fit where γ is the central slope parameter, followed by its pseudo-χ^2 in column 9. Column 10 is the characteristic radius for this two-parameter fit.

Halo	$r_{\rm vir}$ (h^{-1} kpc)	$c_{\rm NFW}$	$\chi^2_{\rm d.o.f.,NFW}$	$c_{\rm M99}$	$\chi^2_{\rm d.o.f.,M99}$	c_γ	$(-)\gamma$	$\chi^2_{\rm d.o.f.}$	$r_{{\rm s},\gamma}$ (h^{-1} kpc)
grp1	705	12.5	4.7	5.5	1.8	7.5	−1.3	0.47	94
cl1	1220	11.5	2.9	5	0.37	6.5	−1.3	0.15	188
gal1	262	18.5	1.2	10	0.98	7.5	−1.6	0.13	35
grp2	530	14.5	0.87	7.5	0.6	4.5	−1.7	0.03	118
dwf0	120	26.5	0.37	14	0.39	14.5	−1.5	0.1	8.3
dwf1	119	28	0.14	15	0.23	18	−1.4	0.04	6.6
cube0	1220	9	0.71	4	1.7	7.5	−1.1	0.08	163
cube1	1190	7	2.4	3	0.88	4	−1.3	0.16	298
cube2	1110	7	0.34	3	2.8	6	−1.1	0.11	185
cube3	1050	10	0.33	4.5	0.84	8.5	−1.1	0.08	124
cube4	1040	7	10.8	3	2.5	1.5	−1.6	0.28	693
cube5	985	11	0.27	5.5	0.63	9.5	−1.1	0.1	104
cube6	933	7.5	3.7	3.5	0.37	2.5	−1.5	0.19	373
cube7	899	7.5	0.097	3.5	2.2	7.5	−1	0.04	120
cube8	892	13	0.15	6.5	0.46	13	−1	0.08	69
cube9	863	12	0.078	6	0.27	10.5	−1	0.02	82
$n=0$	1200	25	0.47	13.5	0.54	14	−1.5	0.14	85
$n=-1$	1190	16	0.16	8.5	0.1	12.5	−1.2	0.04	95
$n=-2$	1120	7.5	0.8	3.5	0.22	4.5	−1.3	0.06	249
$n=-2.7$	635	6	0.26	3	0.51	5.5	−1.1	0.1	163

two-parameter fit produces a visually better fit to the density profile in most cases. The range in $(-)\gamma$ for the $z=0$ haloes is -1 to -1.7. Note that there is a partial degeneracy between γ and the concentration radius. A pseudo (because the data points are correlated) χ^2 per degree of freedom for each of these fits shows substantial improvement over NFW or M99 fits; see Table 2. The profile fits are based on a least squares method, where a Poisson uncertainty is estimated for each point based on the effective number of particles for the density given by the kernel-based profiles, with logarithmically spaced bins.

4.2 Redshift evolution

To gain an understanding of the physical effects that set the inner slope of halo density profiles, we plot the evolution of the profile slope in terms of the $z=0$ virial radius in non-comoving coordinates for our four best haloes. This allows us to ignore the effects that expansion of the universe or evolving $r_{\rm vir}$ have on the power-law slope of the profile. We see in Fig. 6 that the density profile inner slope for each halo evolves very little in non-comoving coordinates, plotted as $\mathrm{d}\ln\rho/\mathrm{d}\ln(r/r_{\rm vir,0})$, a result also found by Fukushige & Makino (2001) and Fukushige et al. (2004). In our cluster CL1, the slope slowly steepens with time at $z \gtrsim 2$, but in our other less massive haloes, the inner density profile slope shows no significant change. The large fluctuation in the profile slope at $z=3$ for the galaxy halo and at $z=5$ for the dwarf halo are most likely owing to the presence of subhaloes that are disrupted earlier. Whatever physical mechanism is responsible for setting the density profile, it must have largely occurred at very high redshift.

The lack of evolution in the physical densities means that the profile of an individual halo is substantially shallower at high redshift in terms of $r/r_{\rm vir}$. Such apparent steepening of the slope with time is merely a scaling issue owing to the growth of the virial radius as mass is added to the outer regions of the halo. Here we note that the profile slope is almost never shallower than the NFW asymptotic value of r^{-1}. Only in the very inner region of our largest cluster CL1 at $z=3$, where the slope trends toward $r^{-0.75}$ at the innermost resolved radius (not plotted), is there a slight hint that NFW slope may be too steep at high redshifts, but this could be simply a result of a subhalo just beyond that radius creating a local density minima, or it could be owing to artificial numerical resolution effects at high redshift where the halo resolution is lower.

4.3 Trends in profile concentration and inner slope

The profile concentration and thus the inner slope at a given radius are predicted by NFW and others to be a function of mass and redshift, when considered in terms of $r/r_{\rm vir}$, with characteristic radius r_s increasing with increasing M/M_*. Here, M_* is the characteristic mass of collapsing haloes defined by the scale at which the rms linear density fluctuation equals the threshold for non-linear collapse [i.e. $\sigma(M_*(z)) = \delta_c$]. We have measured the NFW concentration parameter, $c_{\rm NFW}$, by forcing our profiles to an NFW profile, and performing a least squares fit. In Fig. 7, we plot the concentration parameter for our set of haloes, and we show the Eke et al. (2001) prediction for $c_{\rm NFW}$. The concentration dependence on M/M_* for our haloes is significantly steeper than predicted by NFW for $M < M_*$, and within the scatter of our haloes for $M > M_*$. Measured values of the inner slopes also show clear trends with mass and redshift, shown in Fig. 8, though this is owing, at least in part, to the degeneracy between slope and concentration. Here, we have measured the average value of the power-law slope $\mathrm{d}\ln\rho/\mathrm{d}\ln(r/r_{\rm vir})$ between 2 and 5 per cent $r_{\rm vir}$. The asymptotic inner slope parameter, γ, from a two-parameter fit of γ and concentration as given by equation (3), is plotted in Fig. 9, and has a weak dependence on M/M_* for our haloes, with a large scatter. The median value of γ in our sample trends toward shallower inner slopes with increasing M/M_*, given by

$$\gamma \simeq 1.4 - 0.08\log_{10}(M/M_*), \quad (4)$$

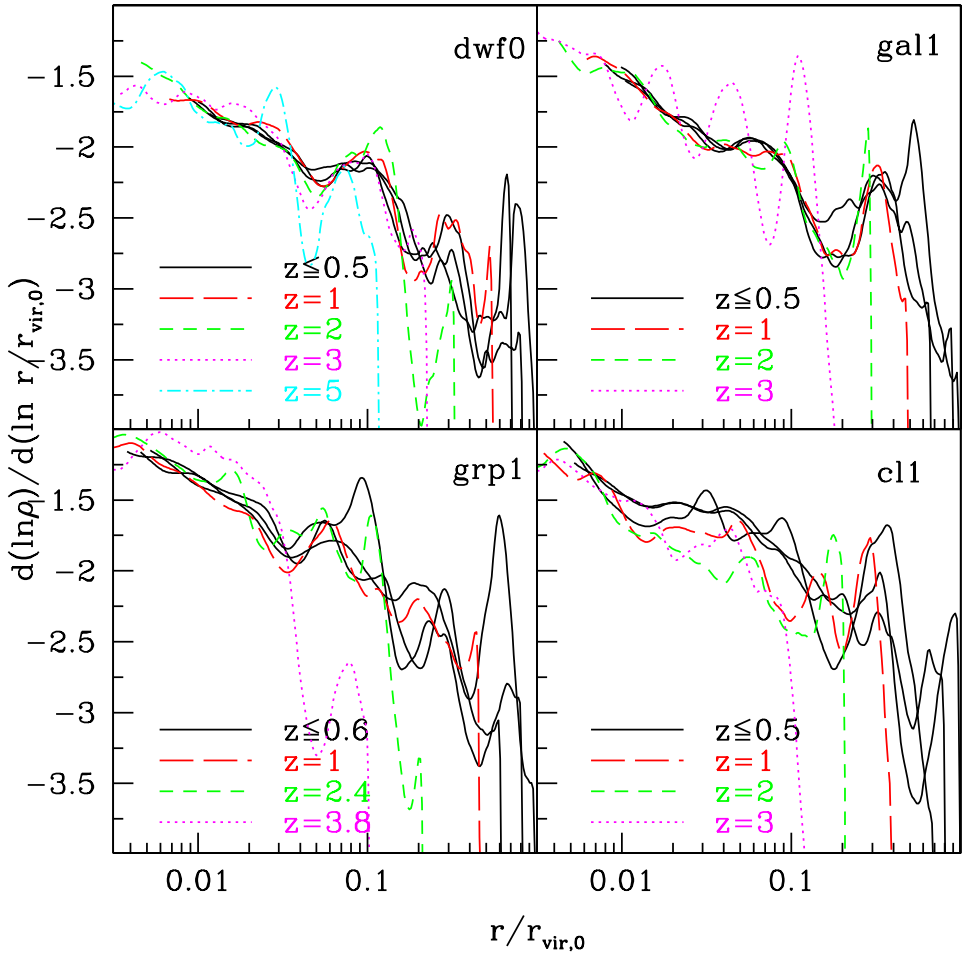

Figure 6. Evolution of the slope of the density profiles of four haloes plotted against $r_{\rm vir}$ at $z = 0$ in non-comoving (physical) coordinates as in Fig. 3. Mass beyond the virial radius of each epoch is ignored. Note that if plotted simply in terms of $r/r_{\rm vir}$ the haloes would appear to flatten with increased redshift.

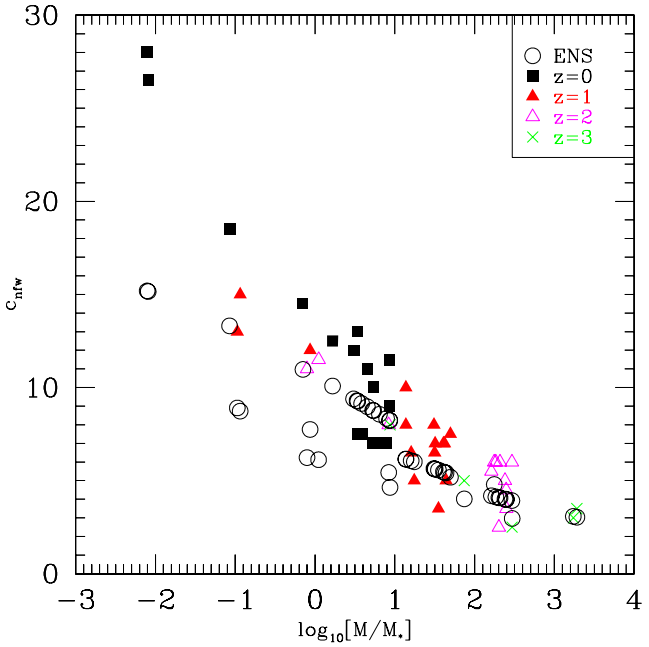

Figure 7. Best-fitting NFW concentration parameter $r_{\rm vir}/r_{\rm s}$ for our set of haloes as a function of M/M_*. Empirical predictions by Eke et al. (2001) are given by open circles.

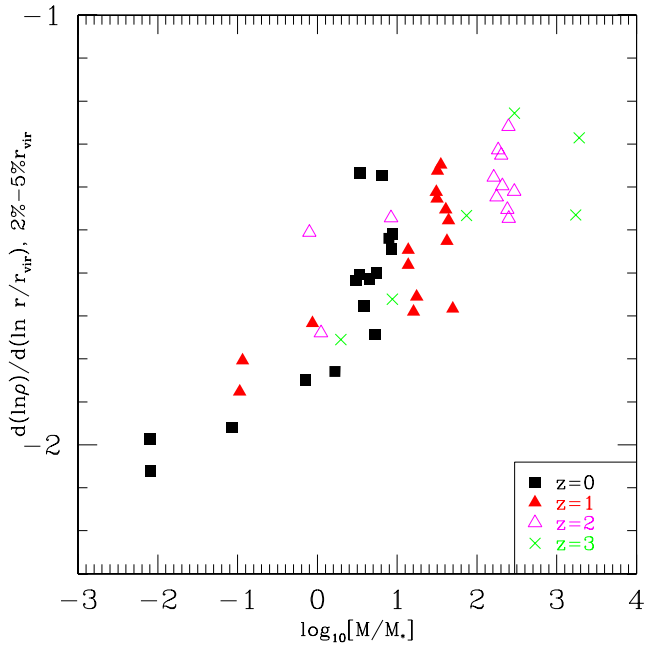

Figure 8. Density profile slopes of our 16 haloes sample averaged over the range of 2–5 per cent $r_{\rm vir}$. Haloes not resolved to 2 per cent $r_{\rm vir}$ are not plotted.

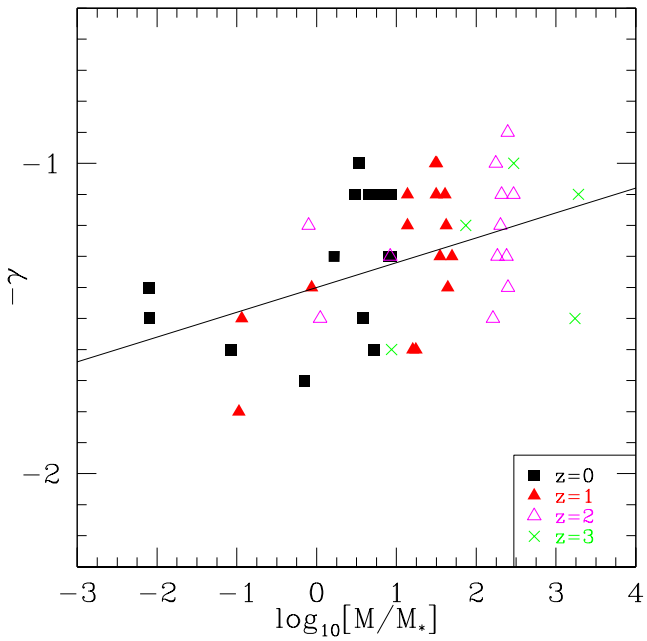

Figure 9. The asymptotic inner slope parameter, γ, from a two-parameter fit of our 16 halo sample. γ and the concentration are both allowed to vary. The solid line fit is given by equation (4).

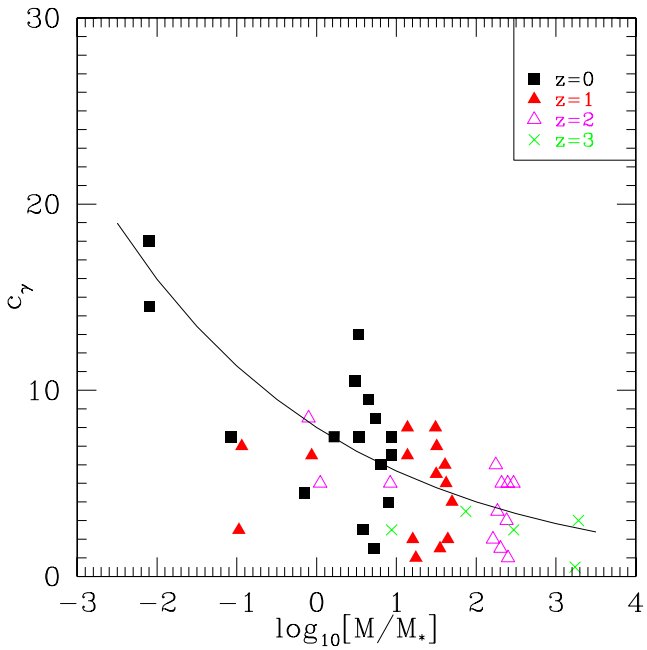

Figure 10. The concentration parameter from a two-parameter fit of our 16 halo sample, c_γ. The asymptotic inner slope parameter, γ, and the concentration are both allowed to vary. The solid line fit is given by equation (5).

with a scatter of $\Delta\gamma \sim \pm 0.3$ for our haloes, and valid for haloes of 0.01 M_*–1000M_*. Fig. 10 shows that the concentration parameter in this two-parameter fit, c_γ, shows a significant trend toward higher values as M/M_* decreases. The trend is weaker and has significantly more scatter than the forced NFW fit $c_{\rm NFW}$ dependence on M/M_* (see Fig. 7). Adopting a power-law parametrization as in e.g. Huffenberger & Seljak (2003), the median c_γ for our haloes is

$$c_\gamma \simeq 8.(M/M_*)^{-0.15}, \quad (5)$$

with a M/M_* dependent scatter roughly equal to $\pm\, c_\gamma$.

4.4 Cosmological variance and stability of profiles

In our CUBEHI simulation, we examine the stability in the profiles of our set of ten clusters over time-scales separated by $\Delta z \simeq 0.01$ for $z \leqslant 0.2$; Fig. 11. In the outer regions, orbiting substructure creates substantial scatter, however, the inner density profile is relatively stable. Thus, differences between the central density profiles of haloes of similar mass reflect different inherent properties of the halo, rather than temporal effects of orbiting substructure.

In the hopes of understanding what physical processes are responsible for setting the central density profile of each halo, we examine the evolution of the main halo and its progenitors. We construct merger histories for each cluster and examine a number of properties, including: evolution of the central cusp mass concentration; cluster accretion history; total collapsed progenitor mass; and angular momentum profiles. To follow the mass accretion history of the cluster and its progenitors, we use the friends-of-friends algorithm (FOF, Davis et al. 1985). To follow the evolution of the mass concentration that makes up the cluster cusp, we use SKID[4] (Stadel 2001), which is able to identify bound mass concentrations independently of environment.

In Fig. 12, we plot the mass evolution of the central SKID progenitor. The two haloes with the earliest forming central SKID halo are also those that have density profiles most closely matching the M99 profile (cube4 and cube6; see Fig. 4, Table 2), both with slopes that steepen slowly toward $r^{-1.5}$, beginning at radii of roughly 10 per cent $r_{\rm vir}$, implying large concentration radii. If not simply a coincidence, then this implies that the central cusp material is assembled earlier in haloes with steeper central slope parameters. We then consider the effects of the mass accretion history of the cluster on the final density profile, and find that accretion history correlates with halo concentration, not with cusp slope. Fig. 13 shows that the three haloes with the highest concentration undergo a phase of rapid growth at $z \simeq 2$–8, making their normalized mass temporarily ∼3 times larger than the other seven clusters, which experience nearly uniform accretion rates. We have also examined the evolution of the total collapsed progenitor mass, and find a similar correlation with cluster concentration. At redshifts of ∼10, the same three highly concentrated haloes have ∼3 times more total mass in collapsed progenitors (not plotted), where we have only considered progenitors of mass greater than 0.01 per cent of the final cluster mass. The correlation of the concentration parameter with halo and progenitor collapse time is not surprising; in fact, as have shown in Section 4.3, lower mass haloes, which are assembled earlier in a hierarchical model, have smaller concentration radii. The concentration trends also qualitatively agree with correlations of formation epoch and concentration found in numerical simulations by Wechsler et al. (2002). However, a cautionary note is needed here. Even though in the CUBEHI simulation, the halo masses differ by only a factor of ∼3 and thus cover a narrow range in median concentration parameter (see equation 5), the two least massive and hence most poorly resolved clusters, are also the two most concentrated. A larger set of higher resolution haloes is needed to conclusively rule out the possibility that haloes resolved with fewer particles (and identical softening) lead to higher concentrations. In Fig. 14, we plot the

[4] SKID available at: http://hpcc.astro.washington.edu.

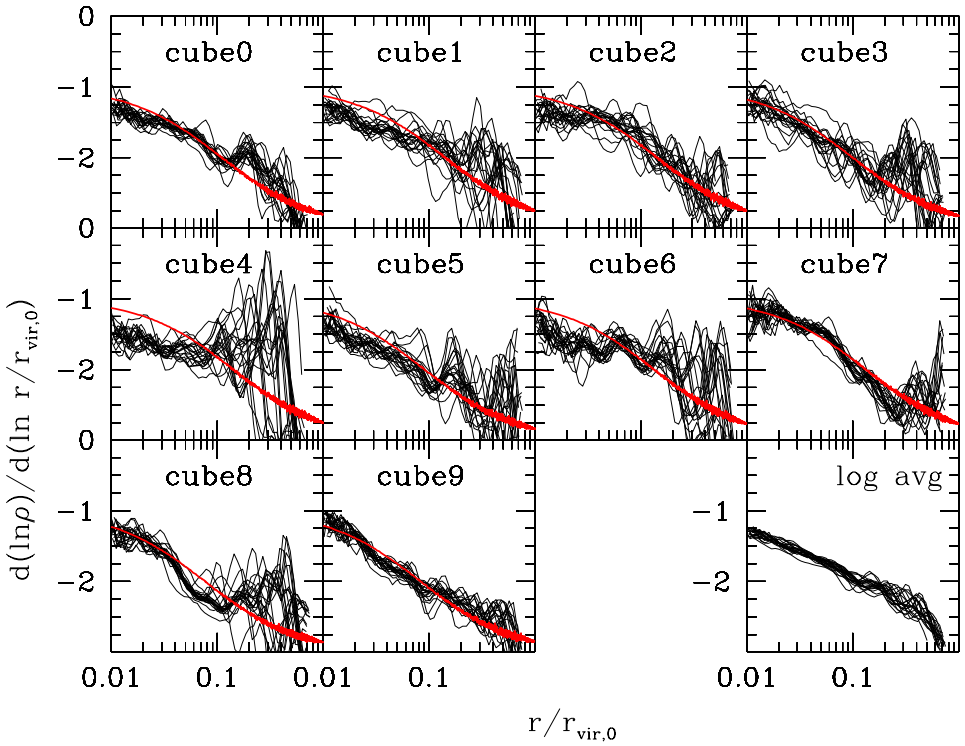

Figure 11. Density profile slopes of our 10 clusters from the CUBEHI simulation. Here we plot the density profile at intervals separated by $\Delta z \simeq 0.01$ up to $z = 0.2$. Note that these profiles are binned, rather than kernel based. From top to bottom and left to right, the haloes are plotted based on descending mass. The lower right-hand plot is the average of the slope value for all 10 clusters. The NFW profile with the best-fitting concentration value is denoted by the solid curve for each halo.

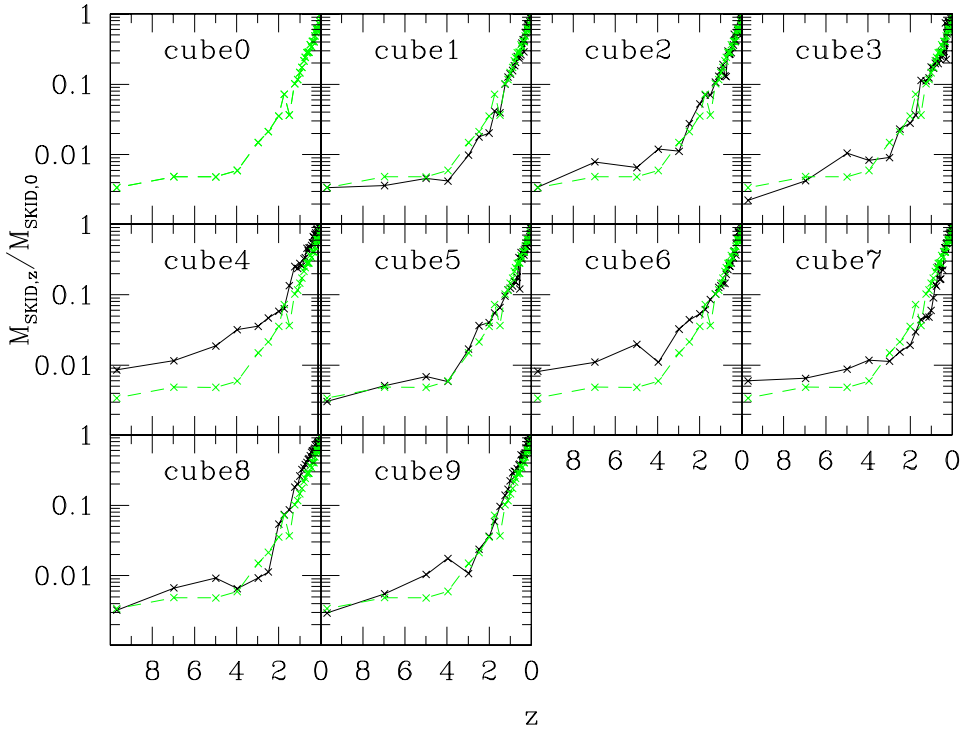

Figure 12. Evolution of the mass of the central SKID progenitor halo for the same 10 clusters as Fig. 11. For reference, the most massive halo is replotted as a dashed curve in each plot window.

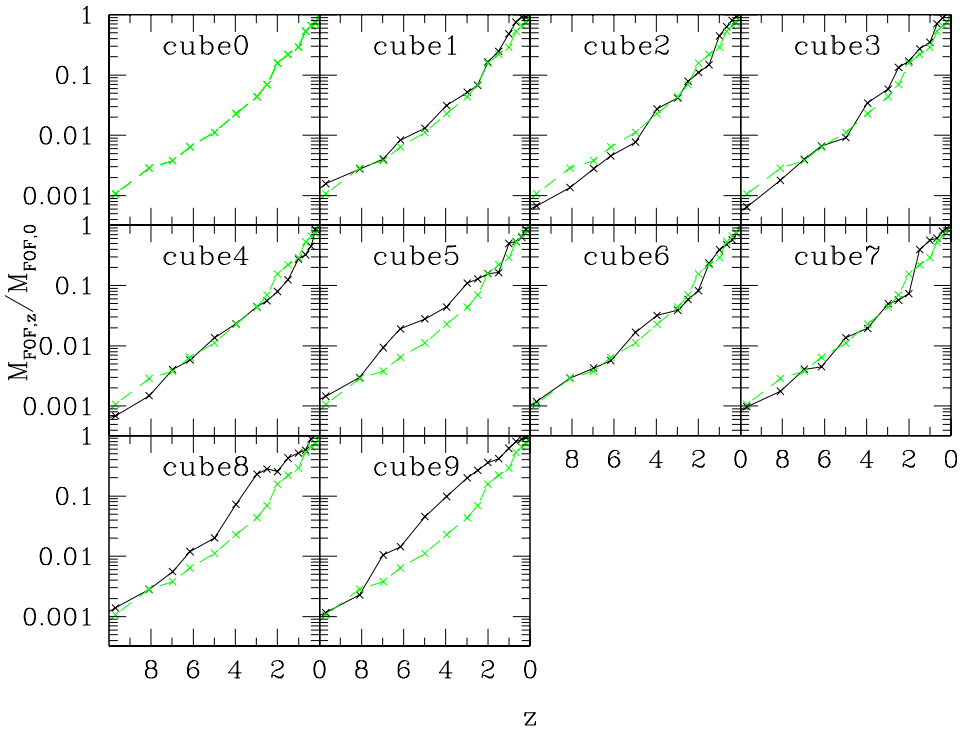

Figure 13. Evolution of the most massive FOF progenitor halo for the same 10 clusters as in Figs 11 and 12. For reference, the most massive halo is plotted as a dashed curve in each plot window.

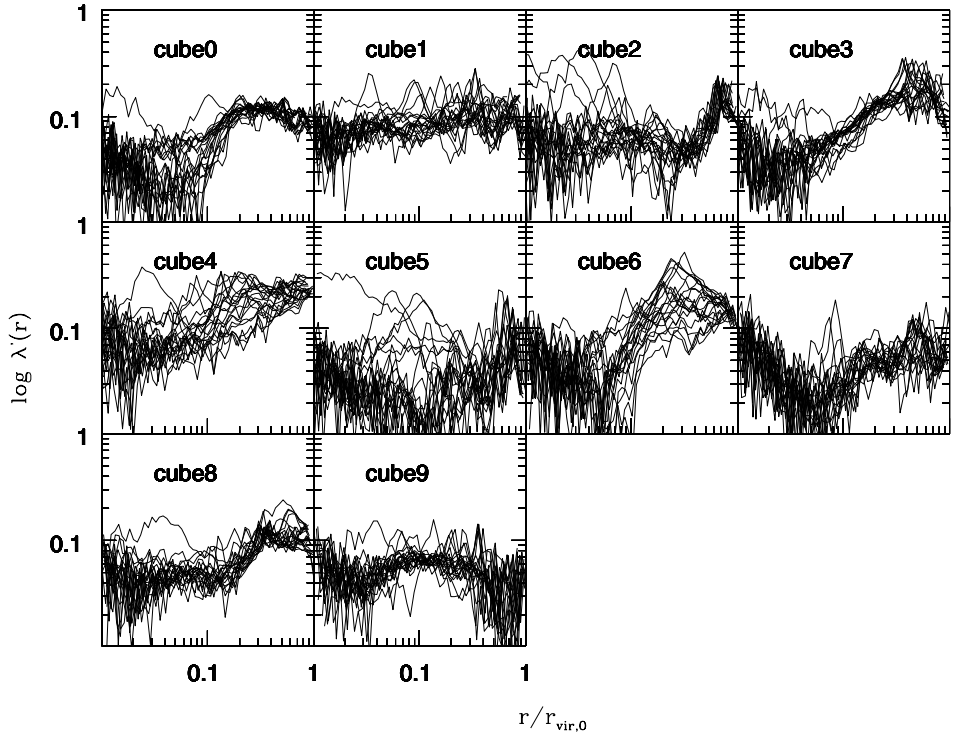

Figure 14. Angular momentum profile of the 10 CUBEHI clusters shown in Figs 11–13.

angular momentum parameter $\lambda' = j/\sqrt{2v_c r}$, from Bullock et al. (2001b), where j is the specific angular momentum. We see no correlation of profile concentration or central slope with λ' in either the inner or the outer regions. We also have examined the angular momentum profiles at high redshift, but find no clear correlation with halo concentration or central slope. This is puzzling given that merger histories, which correlate with the density profiles, should also correlate with the angular momentum distribution.

4.5 Power-law cosmologies

To understand the effects of the power spectral slope index, n, we have simulated the renormalized volume cluster CL1 in scale-free cosmologies with a range of values for n. Here the initial density fluctuation power spectrum is given by $P \propto k^n$, and is normalized to $\sigma_8 = 1.0$ with $\Omega_m = 0.3$ and $\Lambda = 0.7$. Fig. 15 shows the density profile for a cluster with power-law initial conditions given by $n = 0, -1, -2$ and -2.7, followed by the corresponding density profile slopes in Fig. 16. Here we also include plot the Power et al. density criteria as we have not done convergence tests specifically for $P \propto k^n$

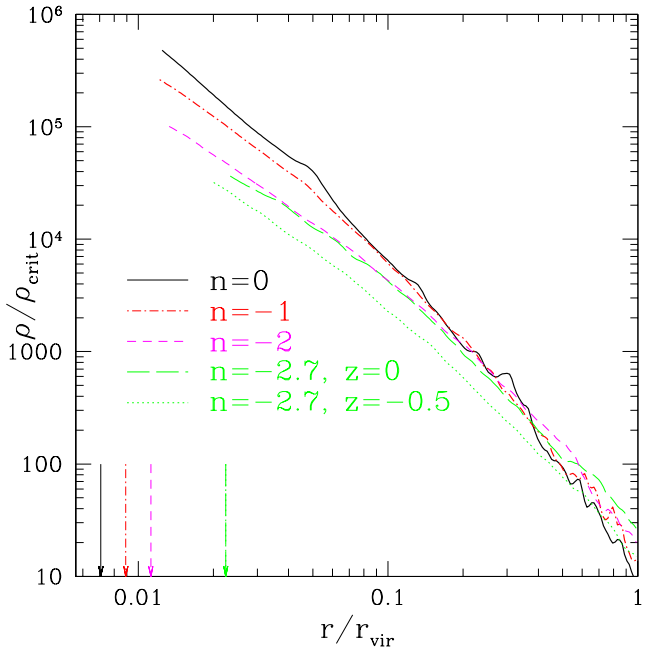

Figure 15. Density profiles for our cluster with initial power spectrum given by $P \propto k^n$ plotted down to $r_{min} = N_p^{-1/3}$ with arrows denoting the Power et al. resolution criteria.

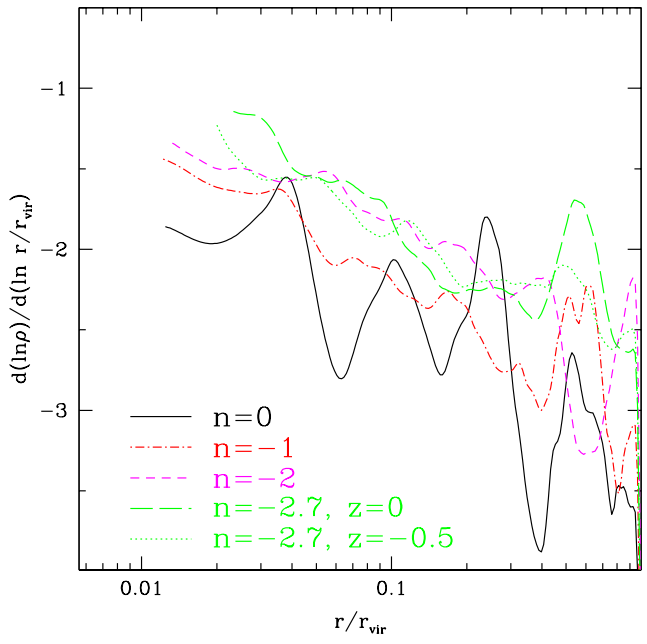

Figure 16. Slopes of the density profiles of Fig. 15, again for our cluster with initial power spectrum given by $P \propto k^n$.

cosmologies. Note that the $n = -2.7$ run has significantly less mass because of the $\sigma_8 = 1.0$ normalization. There is a clear trend that steeper power spectra yield density profiles with flatter slopes and larger concentration radii. Visually, the $n = 0$ cluster displays much more prominent substructure, owing to its proportionally stronger small scale power, with many nearly spherical haloes and few filaments. A two-parameter profile fit yields $\gamma = 1.5$ for $n = 0$ and $\gamma = 1.1$ for $n = -2.7$ (see Table 2). A number of authors (Hoffman & Shaham 1985; Crone, Evrard & Richstone 1994; Cole & Lacey 1996; Syer & White 1998; Navarro et al. 1997; Subramanian et al. 2000; Eke et al. 2001; Huffenberger & Seljak 2003; Ricotti 2003) have suggested a power-law dependence of the density profile that qualitatively agrees with our power-law simulations. However, Syer & White (1998) predict that an $n = -2.7$ power-law cosmology should have an inner slope of $r^{-0.4}$, which is much shallower than seen in our haloes, though not necessarily inconsistent if the slope flattens only at very small radii. The same model predicts an inner slope of $r^{-1.8}$ for the $n = 0$ cosmology, which is very close to the inner slope at the minimum resolved radius of our $n = 0$ halo.

5 DISCUSSION AND CONCLUSIONS

(1) *Density profile trends and the CDM 'cusp problem'.* We follow the evolution of 16 haloes over a large range in parameter space, with masses corresponding to dwarfs through clusters back to $z = 3$ for our highest resolution cluster and $z = 5$ for two dwarfs. By using identical haloes at varying resolution, we have shown that our haloes are likely to be free from biases related to numerical resolution. None of our simulated haloes has a density profile slope significantly shallower than r^{-1} down to the minimum resolved radii of 0.5–2 per cent. These steep cusps are similar to those found in previous CDM simulations, and appear to be in conflict with reported rotation curves from dwarfs and LSBs. Our resolution experiments confirm that steep cusps are formed regardless of numerical resolution, down to the minimum resolved radius of each halo. Previous high-resolution simulations discussed earlier have mostly modelled haloes with masses of $10^{12}\ h^{-1}\ M_\odot$ or higher, leaving the possibility that a mass dependence on the density profile might be able to solve the cusp problem. However, our results show that the observed conflict with ΛCDM density profiles gets worse when considering simulated dwarfs. The enclosed mass at a given radius near the halo core is higher for simulated haloes of lower mass, as the concentration radius is smaller and the measured slope is steeper.

(2) *Convergence of profile slopes.* We confirm that the physical slope of haloes remains stable over time. The inner regions of haloes appear to be composed of mass assembled at very high redshift, implying that present epoch density profiles are determined by the high-redshift merger history. We do see some apparent evolution in the physical slope at very high redshifts for our highest resolution cluster and group. This suggests that for group and cluster-sized haloes, events occurring at $z \simeq 2$–4 are partly responsible for determining the final shape of the density profile, while galaxies and smaller mass haloes have their inner density profile shape almost entirely determined at higher redshifts. The progenitor region of the host halo, owing to its large-scale density enhancement, is the likely site of early-forming small haloes, many of which will merge to form the cusp. After the universe has expanded by a few factors as the cusp material is assembled, the characteristic densities of haloes merging into the main halo should be lower than typical densities within the main cusp, owing to their generally later assembly epoch. Consequently, merging subhaloes will likely be disrupted before dynamical friction can bring them near the centre of the main halo,

where they can affect the central density profile. In this scenario, halo density profiles could converge to roughly flat profiles (in terms of $r/r_{\rm vir}$) at extremely high redshifts. CDM haloes at low redshift might then be expected to have a very small flat inner core, but at radii much less than the inner $\sim$1 per cent that can be currently probed by simulations or observations.

(3) *Lessons from the power-law cosmologies.* The dependence of the concentration parameter on M/M_* is most likely the result of a mechanism analogous to what sets the dependence of concentration on the spectral slope in our power-law cosmologies. In the power-law cosmologies, the ratio of local small-scale to large-scale power depends primarily on the spectral index. When there is lots of small-scale power, the central density profile is generally steeper at any specific radius than when there is little small-scale power. In the case of a shallow spectral index, subhaloes form early, which implies that they have small characteristic radii and thus large characteristic densities, whereas steep spectral indices have late-forming subhaloes. Similar formation epoch arguments can also explain the steeper profiles of small M/M_* haloes. For smaller M/M_* haloes, many subhaloes should form earlier relative to their hosts, as the subhaloes lie at lower σ fluctuations in the density field relative to the local fluctuation on the scale of the host halo. Alternatively, smaller M/M_* haloes, which generally form earlier, and hence when the mean density of the universe is evolving more rapidly, will have subhaloes and cusp material assembled over a wider range of densities than for large M/M_* haloes. Haloes with small M/M_* are thus similar to haloes with a shallow spectral index, because they have subhaloes that form earlier at higher densities relative to the host halo. In models where the inner slope is formed from disrupted subhaloes infalling via dynamical friction, lots of small-scale power should give the main halo a larger concentration parameter. In fact, when there are lots of dense subhaloes more of them will be able to reach closer to the core, steepening the halo nearer to the centre.

(4) *Is there an asymptotic cusp?* A strength of the NFW profile, is that varying just the concentration radius can yield reasonable fits to haloes with very different inner slopes at scales currently resolved by simulations. However, there are no compelling theoretical arguments that the halo profile converges to a slope of r^{-1} at smaller radii. The analytical models mentioned in the introduction imply that the core slope should be a function of M/M_* or power spectral slope. It is possible, and theoretically motivated, that haloes of higher M/M_* or steeper spectral slope than what we have simulated here would actually have a shallower slope than r^{-1}, which would be inconsistent with the NFW profile. Most of our haloes have density profiles that get ever shallower with decreasing radius down to our minimum resolved radius, although they are still consistent with asymptotic cusp slopes of r^{-1} or steeper. Additionally, a few of our haloes appear to have converged to slopes at $r^{-1.5}$ or steeper, which would be inconsistent with the NFW profile, though because of the degeneracy between central slope and concentration parameter, the NFW profile is not definitively ruled out. Simulations of haloes with very high M/M_*, very steep power spectral indices, or orders of magnitude more particles able to probe much farther inward, should be able to test whether or not the r^{-1} NFW central slope corresponds to a minimum possible slope set by the physical processes of CDM halo formation. Navarro et al. (2004) recently proposed a new profile form based on fits to a set of high-resolution haloes. The Navarro et al. profile differs from ours in that it has no asymptotic cusp, but instead continually flattens with decreasing radius. It does not become shallower than r^{-1} until radii smaller than currently resolvable, so it is generally consistent with most of our haloes. However, our profile form is more flexible in that it is able to better match haloes that have steep asymptotic cusps with large concentration radii, and is still a good match to those haloes that continuously flatten down to the minimum resolved radii in our simulations. Future simulations will likely need to probe below $\sim 0.001 r_{\rm vir}$ to determine whether dark haloes have an asymptotic central cusp. The mass distribution at such small radii has a strong effect on the flux of hypothesized dark matter annihilation signals that may be detectable via γ-rays from the galactic centre (e.g. Stoehr et al. 2003; Evans, Ferrer & Sarkar 2004).

(5) *Profile scatter and the two-parameter profile*. When we plot our haloes with the best-fitting concentration parameters, neither the NFW nor the M99 function provide a good fit to all of the haloes. However, because each halo has a unique profile determined by poorly understood and complex high-redshift events, any possible single parameter profile will be unlikely to fully describe all haloes. Our two-parameter fit describes the general trends with M/M_*, providing a significant improvement over NFW and M99, but it still does not account for the large halo to halo scatter at a given mass and redshift. Our evidence in the CUBEHI clusters for a likely correlation between the cusp material assembly epoch and cusp slope, and between halo accretion history and concentration radius, suggests that the density profiles might be, at least partly, determined from the evolutionary history of the progenitor haloes and substructures clumps. Larger sets of high-resolution haloes should be able to quantify the role of mergers and other stochastic processes in shaping the density profile.

ACKNOWLEDGMENTS

We are grateful to the anonymous referee for helpful and constructive comments and suggestions. We thank Lucio Mayer for assistance with one of the runs. DR has been supported by the NASA Graduate Student Researchers Program. DR was partly supported by PPARC. FG is a David E. Brooks Research Fellow. FG was partly supported by NSF grant no. AST-0098557 at the University of Washington. TRQ was partly supported by the National Science Foundation. Simulations were performed on the Origin 2000 at NCSA and NASA Ames, the IBM SP4 at the Arctic Region Supercomputing Centre (ARSC) and at CINECA (Bologna, Italy), the NASA Goddard HP/Compaq SC 45, and at the Pittsburgh Supercomputing Centre. We thank Chance Reschke for dedicated support of our computing resources, much of which were graciously donated by Intel.

REFERENCES

Abramson I. S., 1982, Ann. Stat. 10, 1217
Bardeen J. M., Bond J. R., Kaiser N., Szalay A. S., 1986, ApJ, 305, 15
Bennett C. L. et al., 2003, ApJS, 148, 97B
Bentley J. L., 1975, Commun. ACM, 18, 9
Bullock J. S., Kolatt T. S., Sigad Y., Somerville R. S., Kravtsov A. V., Klypin A. A., Primack J. R., Dekel A., 2001a, MNRAS, 321, 559
Bullock J. S., Dekel A., Kolatt T. S., Kravtsov A. V., Klypin A. A., Porciani C., Primack J. R., 2001b, ApJ, 555, 240
Cole S., Lacey C., 1996, MNRAS, 281, 716
Crone M., Evrard A., Richstone D., 1994, ApJ, 434, 402
Davis M., Efstathiou G., Frenk C. S., White S. D. M., 1985, ApJ, 292, 381
de Blok W. J., McGaugh S. S., Bosma A., Rubin V. C., 2001, ApJ, 552, L23
Diemand J., Moore B., Stadel J., Kazantzidis S., 2004, MNRAS, 348, 977
Eke V. R., Cole S., Frenk C. S., 1996, MNRAS, 282, 263
Eke V. R., Navarro J. F., Steinmetz M., 2001, ApJ, 554, 114
Evans N. W., Ferrer F., Sarkar S., 2004, Phys. Rev. D, 69, 123501
Flores R. A., Primack J. R., 1994, ApJ, 427, L1
Fukushige T., Makino J., 1997, ApJ, 477, L9

Fukushige T., Makino J., 2001, ApJ, 557, 533
Fukushige T., Makino J., 2003, ApJ, 588, 674
Fukushige T., Kawai A., Makino J., 2004, ApJ, 606, 625
Gavazzi R., Fort B., Mellier Y., Pello R., Dantel-Fort M., 2003, A&A, 403, 11
Gentile G., Salucci P., Klein U., Vergani D., Kalberla P., 2004, MNRAS, 351, 903
Ghigna S., Moore B., Governato F., Lake G., Quinn T., Stadel J., 1998, MNRAS, 300, 146
Ghigna S., Moore B., Governato F., Lake G., Quinn T., Stadel J., 2000, 544, 616
Governato F., Ghigna S., Moore B., 2001, ASP Conf. Ser. 245, Astrophysical Ages and Times Scales. Astron. Soc. Pacific, San Francisco, p. 469
Hayashi E. et al., 2004, MNRAS, 355, 794
Hernquist L., 1990, ApJ, 356, 359
Hoffman Y., Shaham J., 1985, ApJ, 297, 16
Huffenberger K. M., Seljak U., 2003, MNRAS, 340, 1199
Huss A., Jain B., Steinmetz M., 1999, ApJ, 517, 64
Jimenez R., Verde L., Oh P., 2003, MNRAS, 339, 243
Jing Y. P., Suto Y., 2000, ApJ, 529, L69
Jing Y. P., Suto Y., 2002, ApJ, 574, 538
Katz N., White S., 1993, ApJ, 412, 478
Klypin A., Kravtson A. V, Bullock J. S., Primack J. R., 2001, ApJ, 554, 903
Lacey C., Cole S., 1994, MNRAS, 271, 676
Lake G., 1989, AJ, 98, 1253
Lewis A. D., Buote D. A., Stock J. T., 2003, ApJ, 586, 135
Merritt D., 1994, http://www.rit.edu/∼drmsps/inverse.html
Merritt D., Tremblay B., 1994, AJ, 108, 514
Moore B., 1994, Nat, 370, 629
Moore B., Governato F., Quinn T., Stadel J., Lake G., 1998, AJ, 499, L5 (M98)
Moore B., Quinn T., Governato F., Stadel J., Lake G., 1999, MNRAS, 310, 1147 (M99)
Moore B., Calcaneo-Roldan C., Stadel J., Lake G., Sebastiano G., Governato G., 2001, Phys. Rev. D, 64, 063508
Navarro J. F., Frenk C. S., White S. D. M., 1996, ApJ, 462, 563 (NFWa)
Navarro J. F., Frenk C. S., White S. D. M., 1997, ApJ, 490, 493 (NFWb)
Navarro J. F. et al., 2004, MNRAS, 349, 1039
Power C., Navarro J. F., Jenkins A., Frenk C. S., White S. D. M., Springel V., Stadel J., Quinn T., 2003, MNRAS, 338, 14
Press W. H., Schechter P., 1974, ApJ, 187, 425
Reed D., Gardner J., Quinn T., Stadel J., Fardal M., Lake G., Governato F., 2003, MNRAS, 346, 565
Ricotti M., 2003, MNRAS, 344, 1237
Salucci P., 2003, astro-ph/0310376
Salucci P., Burkert A., 2000, ApJ, 537, L9
Sand D. J., Treu T., Ellis R. S., 2002, ApJ, 574, L129
Sand D. J., Treu T., Smith G. P., Ellis R. S., 2004, ApJ, 604, 88
Scott D. W., 1992, Multivariate Density Estimation. John Wiley and Sons, New York, p. 130
Shapiro P. R., Iliev I. T., 2000, ApJ, 542L, 1
Simon J., Bolatto A., Leroy A., Blitz L., 2003, ApJ, 596, 957
Spergel D. et al., 2003, ApJS, 148, 175
Splinter R., Melott A., Shandarin S., Suto Y., 1998, ApJ, 497, 38
Stadel J., 2001, PhDT
Stoehr F., White S., Springel V., Tormen G., Yoshida N., 2003, MNRAS, 345, 1313
Subramanian K., Cen R., Ostriker J. P., 2000, ApJ, 538, 528
Syer D., White S. D. M., 1998, MNRAS, 293, 337
Tasitsiomi A., Kravtsov A., Gottlober S., Klypin A., 2004, ApJ, 607, 125
Taylor J., Navarro J., 2001, ApJ, 563 483
Tremaine S., Gunn J., 1979, Phys. Rev. Lett., 42, 407
Tyson J. A., Kochanski G. P., Dell'Antontio I. P., 1998, ApJ, 498, L107
van den Bosch F., Swaters R., 2001, MNRAS, 325, 1017
van den Bosch F. C., Robertson B. E., Dalcanton J. J., de Blok W. J. G., 2000, AJ, 119, 1579
Wadsley J., Stadel J., Quinn T., 2004, New Astron., 9, 137
Wechsler R. H., Bullock J. S., Primack J. R., Kravtsov A. V., Dekel A., 2002, ApJ, 568, 52
Zhao H. S., 1996, MNRAS, 278, 488

APPENDIX A: KERNEL ROUTINE FOR DENSITY PROFILE ESTIMATION

Here we present the algorithms which we used to derive smooth estimates, $\hat{\nu}(r)$ and $\hat{\Sigma}(R)$, of the particle number density and surface density profiles from the N-body positions.

The routines in MAPEL (Merritt 1994) allow one to derive maximally unbiased estimates of ν and Σ using penalty functions that embody the approximate power-law nature of these functions. However, the MAPEL routines are relatively slow, and this fact presented difficulties when constructing estimates using the $N \sim 10^6$ particle data sets. Kernel based algorithms are faster but potentially more biased; however, we found that density profiles produced with MAPEL and kernel methods are in excellent agreement down to our minimum resolved radii. Thus we have used the kernel estimator in our analyses.

Our derivation follows that in Merritt & Tremblay (1994). In the absence of any symmetries in the particle distribution, a valid estimate of the number density ν corresponding to a set of particle positions $\boldsymbol{r}_i$ (see Fig. A1) is

$$\hat{\nu}(\boldsymbol{r}) = \sum_{i=1}^{N} \frac{1}{h^3} K\left[\frac{1}{h}\,|\boldsymbol{r} - \boldsymbol{r}_i|\right], \tag{A1}$$

where h is the window width and K is a normalized kernel, e.g. the Gaussian kernel

$$K(y) = \frac{1}{(2\pi)^{3/2}} \exp^{-y^2/2}. \tag{A2}$$

Now imagine that each particle is smeared uniformly around the surface of the sphere whose radius is r_i and whose origin is at (0,0,0). If the density profile is actually spherically symmetric, this smearing will leave the density unchanged; if not, it will produce a spherically symmetric approximation to the true profile. The spherically

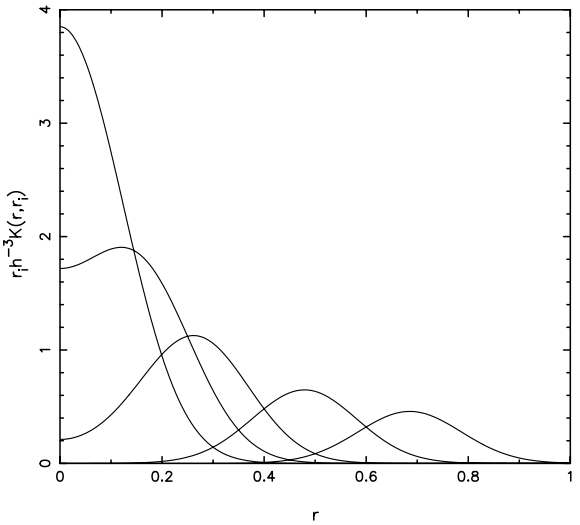

Figure A1. Kernels for the radial density estimation problem. Window width is $h = 0.1$ and particles are located at $r = (0.1, 0.2, 0.3, 0.5, 0.7)$.

symmetrized density estimate is

$$\hat{\nu}(r) = \sum_{i=1}^{N} \frac{1}{h^3} \frac{1}{4\pi} \int \mathrm{d}\phi \int \mathrm{d}\theta \ \sin\theta \ K\left(\frac{d}{h}\right), \tag{A3a}$$

$$d^2 = |\boldsymbol{r} - \boldsymbol{r}_i|^2 \tag{A3b}$$

$$= r_i^2 + r^2 - 2rr_i\cos\theta, \tag{A3c}$$

where θ is defined (arbitrarily) from the $\boldsymbol{r}_i$-axis. This may be written in terms of the angle-averaged kernel $\tilde{K}$:

$$\hat{\nu}(r) = \sum_{i=1}^{N} \frac{1}{h^3} \tilde{K}(r, r_i, h), \tag{A4a}$$

$$\tilde{K}(r, r_i, h) \equiv \frac{1}{4\pi} \int \mathrm{d}\phi \int \mathrm{d}\theta \ \sin\theta \ K \times \left(h^{-1}\sqrt{r_i^2 + r^2 - 2rr_i\cos\theta}\right) \tag{A4b}$$

$$= \frac{1}{2} \int_{-1}^{1} \mathrm{d}\mu \ K\left(h^{-1}\sqrt{r_i^2 + r^2 - 2rr_i\mu}\right). \tag{A4c}$$

Substituting for the Gaussian kernel, we find

$$\tilde{K}(r, r_i, h) = \frac{1}{(2\pi)^{3/2}} \left(\frac{rr_i}{h^2}\right)^{-1} \times \mathrm{e}^{-(r_i^2+r^2)/2h^2} \sinh(rr_i/h^2). \tag{A4}$$

A better form for numerical computation is

$$\tilde{K}(r, r_i, h) = \frac{1}{2(2\pi)^{3/2}} \left(\frac{rr_i}{h^2}\right)^{-1} \times \left[\mathrm{e}^{-(r_i-r)^2/2h^2} - \mathrm{e}^{-(r_i+r)^2/2h^2}\right]. \tag{A5}$$

We want to vary the window width with position in such a way that the bias-to-variance ratio of the estimate is relatively constant. Let h_i be the window width associated with the ith particle. The density estimate based on a variable window width is

$$\hat{\nu}(r) = \sum_{i=1}^{N} \frac{1}{h_i^3} \tilde{K}(r, r_i, h_i). \tag{A6}$$

The optimal way to vary h_i is according to the rule of Abramson (1982)

$$h_i \propto \nu^{-\alpha}(r_i), \quad \alpha = 1/2. \tag{A7}$$

As we do not know $\nu(r)$ a priori, we instead varied h_i according to

$$h_i \propto r^{\beta}. \tag{A8}$$

We found that $\beta = 1/2$ gave good results, which is reasonable as density profiles are close to $\nu \sim r^{-1}$. One could improve on this by first constructing a pilot estimate of ν then using Abramson's rule.

The surface density profile could be computed via simple projection of $\hat{\nu}(r)$. Instead, we computed $\hat{\Sigma}(R)$ directly from the coordinates projected along one axis. The two-dimensional kernel estimate of $\Sigma(\boldsymbol{R})$ in the absence of any symmetries is

$$\hat{\Sigma}(\boldsymbol{R}) = \sum_{i=1}^{N} \frac{1}{h^2} K'\left[\frac{1}{h}\,|\boldsymbol{R} - \boldsymbol{R}_i|\right], \tag{A9}$$

where K' is the two-dimensional Gaussian kernel,

$$K'(y) = \frac{1}{2\pi}\mathrm{e}^{-y^2/2}. \tag{A10}$$

Now smear each particle uniformly in angle ϕ at fixed R_i. The density estimate becomes

$$\hat{\Sigma}(R) = \sum_{i=1}^{N} \frac{1}{h^2} \frac{1}{2\pi} \int K'\left(\frac{d}{h}\right) \mathrm{d}\phi, \tag{A11a}$$

$$d^2 = R_i^2 + R^2 - 2RR_i\cos\phi. \tag{A11b}$$

In terms of the angle-averaged kernel $\tilde{K}'$:

$$\hat{\Sigma}(R) = \sum_{i=1}^{N} \frac{1}{h^2} \tilde{K}'(R, R_i, h), \tag{A12a}$$

$$\tilde{K}'(R, R_i, h) \equiv \frac{1}{2\pi} \int K'\left(h^{-1}\sqrt{R_i^2 + R^2 - 2RR_i\cos\phi}\right) \mathrm{d}\phi \tag{A12b}$$

$$= \frac{1}{2\pi}\mathrm{e}^{-(R_i^2+R^2)/2h^2} I_0(RR_i/h^2), \tag{A12c}$$

where the last expression was derived using the Gaussian kernel; I_0 is the modified Bessel function.

This paper has been typeset from a TEX/LATEX file prepared by the author.